# Multi-Frequency mmWave Massive MIMO Channel Measurements and Characterization for 5G Wireless Communication Systems

Jie Huang, Cheng-Xiang Wang, *Fellow, IEEE*, Rui Feng, Jian Sun, *Member, IEEE*,
Wensheng Zhang, *Member, IEEE*, and Yang Yang, *Senior Member, IEEE*

***Abstract*— Most millimeter wave (mmWave) channel measurements are conducted with different configurations, which may have large impacts on propagation channel characteristics. In addition, the comparison of different mmWave bands is scarce. Moreover, mmWave massive multiple-input multiple-output (MIMO) channel measurements are absent, and new propagation properties caused by large antenna arrays have rarely been studied yet. In this paper, we carry out mmWave massive MIMO channel measurements at 11-, 16-, 28-, and 38-GHz bands in indoor environments. The space-alternating generalized expectation-maximization algorithm is applied to process the measurement data. Important statistical properties, such as average power delay profile, power azimuth profile, power elevation profile, root mean square delay spread, azimuth angular spread, elevation angular spread, and their cumulative distribution functions and correlation properties, are obtained and compared for different bands. New massive MIMO propagation properties, such as spherical wavefront, cluster birth-death, and non-stationarity over the antenna array, are validated for the four mmWave bands by investigating the variations of channel parameters. Two channel models are used to verify the measurements. The results indicate that massive MIMO effects should be fully characterized for mmWave massive MIMO systems.**

Manuscript received November 11, 2016; revised February 22, 2017; accepted March 9, 2017. Date of publication April 28, 2017; date of current version June 19, 2017. This work was supported in part by the EU H2020 ITN 5G Wireless Project under Grant 641985, in part by the EU FP7 QUICK Project under Grant PIRSES-GA-2013-612652, in part by the EPSRC TOUCAN Project under Grant EP/L020009/1, in part by the National Science and Technology Major Project under Grant 2014ZX03003012-001, and in part by the Natural Science Foundation of China under Grant 61210002 and Grant 61371110, in part by the Ministry of Science and Technology (MOST) 863 Hi-Tech Program under Grant 2015AA01A702, and in part by the Science and Technology Commission of Shanghai Municipality (STCSM) under Grant 16510711600. *(Corresponding author: Cheng-Xiang Wang.)*

J. Huang, R. Feng, J. Sun, and W. Zhang are with the Shandong Provincial Key Laboratory of Wireless Communication Technologies, School of Information Science and Engineering, Shandong University, Jinan 250100, China (e-mail: hj_1204@sina.cn; fengxiurui604@163.com; sunjian@sdu.edu.cn; zhangwsh@sdu.edu.cn).

C.-X. Wang is with the Shandong Provincial Key Laboratory of Wireless Communication Technologies, School of Information Science and Engineering, Shandong University, Jinan 250100, China, and also with the Institute of Sensors, Signals and Systems, School of Engineering and Physical Sciences, Heriot-Watt University, Edinburgh EH14 4AS, U.K. (e-mail: cheng-xiang.wang@hw.ac.uk).

Y. Yang is with the Key Laboratory of Wireless Sensor Network and Communication, Shanghai Institute of Microsystem and Information Technology, Chinese Academy of Sciences, Shanghai 200050, China, and also with the Shanghai Research Center for Wireless Communications, Shanghai 201210, China (e-mail: yang.yang@wico.sh).

Color versions of one or more of the figures in this paper are available online at http://ieeexplore.ieee.org.

Digital Object Identifier 10.1109/JSAC.2017.2699381

***Index Terms*— Millimeter wave, massive MIMO, SAGE, channel measurements, channel models.**

## I. INTRODUCTION

MILLIMETER wave (mmWave) communication has been considered as a key technology for the fifth generation (5G) wireless communications, e.g., for wide-band cellular communication (hotspot and small cell), wireless backhaul, indoor, and device-to-device (D2D) communications [1], [2]. MmWave generally corresponds to 30–300 GHz frequency bands, but sometimes 10–30 GHz bands are also included as they share some similar propagation characteristics. Compared with sub-6 GHz frequency bands, mmWave bands have large available bandwidths but suffer from additional high path loss. Recently, many groups and standardization organizations including METIS [3], MiWEBA [4], mmMAGIC [5], 5GCM [6], 3GPP 38.900 [7], IEEE 802.11 NG60 [8], and NYU Wireless [9] have tried to develop mmWave channel models for the frequency range of 6–100 GHz.

Various channel measurements have been conducted at some popular mmWave bands, such as 11, 15, 28, 38, 45, 60, and 73 GHz bands. In [10], 11 GHz outdoor urban cellular channel measurements were conducted by using a 24×24 multiple-input multiple-output (MIMO) channel sounder with 400 MHz bandwidth and dual-polarized 12-element uniform circular arrays. Path loss, shadowing, cell coverage, polarization properties, and root mean square (RMS) delay spread (DS) were obtained. In [11], 15 GHz channel measurements were conducted in two indoor corridor environments by using a vector network analyzer (VNA) and a spectrum analyzer with 1 GHz bandwidth. The large-scale fading, K-factor, and RMS DS were obtained. In [12], a VNA and two high gain horn antennas were used to measure the 28 GHz indoor environments with 1 GHz bandwidth. Power delay profile (PDP), path loss, RMS DS, and power angular profile were obtained. In [13], a sliding correlator based direction-scan-sounding method was used to measure 28 GHz indoor office environments with 500 MHz bandwidth. Both line-of-sight (LOS) and non-line-of-sight (NLOS) scenarios were considered, and the space-alternating generalized expectation-maximization (SAGE) algorithm was applied to estimate delay and angular parameters of multipath components (MPCs). Hur *et al.* [14] conducted 28 GHz measurements in an urban environment with 250 MHz bandwidth. The transmitter (Tx) antenna was scanned in both azimuth and elevation angle domains. The omni-directional PDPs were synthesized. In [15], a commercial backhaul equipment was used to conduct 38 GHz measurements in urban outdoor and outdoor-to-indoor environments. The LOS propagation, reflection, scattering, diffraction, transmission, as well as polarization effects were studied. Zhu *et al.* [16] measured the indoor conference room, cubicle office, and living room at 45 GHz by using a VNA and a signal generator. Path loss exponent, shadowing fading deviation, and cross polarization discrimination ratio were obtained and compared in different scenario setups. Wyne *et al.* [17] measured the 60 GHz channel with 4 GHz bandwidth in indoor conference room and office environments. At both sides of Tx and receiver (Rx), virtual planar array was utilized to investigate the influence of array size on beamforming performance. Haneda [18] conducted 60 and 70 GHz measurements by using a VNA and a signal generator in large office rooms, shopping mall, and station scenarios. Prof. T. S. Rappaport *et al.* from New York University had also conducted various channel measurements at 28, 38, 60, and 73 GHz in campus, base station-mobile access, peer-to-peer, and vehicular scenarios [19]–[21].

However, most of the channel measurements were conducted with different configurations, including measurement environments, channel sounders, antennas, and even post-processing methods, which may have large impacts on propagation channel characteristics. It is hard to have a fair evaluation of different measurement results, though it is very important for the development of a unified channel model framework for large mmWave bands. The comparison of channel propagation characteristics at different mmWave bands is also scarce. Moreover, mmWave massive MIMO channel measurements are scarce in the literature.

Massive MIMO or large antenna array system has the capability of greatly improving spectral efficiency, energy efficiency, and system robustness [22], [23]. In a typical massive MIMO system, single-antenna mobile stations (MSs) communicate with a base station (BS) equipped with a large number of antennas [24]. Due to the increasing number of antennas, the propagation channel characteristics have some new properties and should be measured [25]. In [26], 2.6 GHz outdoor channel measurements were conducted by using a VNA and a 128-element virtual uniform linear array (ULA). It showed that the received power varied over the array significantly, and near field effects and non-stationarity over the array helped to decorrelate the channels for different users. In [27], 2.6 GHz outdoor channel measurements were conducted for a 128-element real cylindrical patch antenna array with a RUSK channel sounder, and for a 128-element virtual ULA with a VNA. In [28], 3.33 GHz outdoor channel measurements were conducted by using a signal generator, a spectrum analyzer, and a 64-element virtual ULA. The non-stationarity of the channel over the array was identified in both delay and spatial domains.

The combination of mmWave and massive MIMO has the potential to dramatically improve wireless access and throughput performance. Such systems benefit from large available signal bandwidth and small antenna form factor. The systems also have advantages in terms of compact dimensions, energy efficiency, flexibility, and adaptivity that would make them ideally suited for 5G communication systems [29]–[32] including high-speed railway systems [33], [34]. As shown in [32], large antenna arrays can be used in mmWave systems to keep the antenna aperture constant, eliminate the frequency dependence of path loss relative to omnidirectional antennas, and provide array gains to counter the larger thermal noise bandwidth. The combination also brings new challenges to channel modeling. Table I shows the main different properties between mmWave massive MIMO channels and conventional wireless channels.

TABLE I

DIFFERENT PROPERTIES BETWEEN mmWAVE MASSIVE MIMO CHANNELS AND CONVENTIONAL WIRELESS CHANNELS

| Properties | MmWave massive MIMO channel | Conventional wireless channel |
|---|---|---|
| Frequency range | 6–100 GHz | Below 6 GHz |
| Bandwidth | On the order of GHz | Smaller than 100 MHz |
| Antenna elements | Up to thousands | Usually less than 10 |
| Wavefront | Spherical wavefront | Plane wavefront |
| Stationarity | Non-stationary | Wide sense stationary |

Recently, a 48-element active phased array antenna was used to measure massive MIMO channels at 44 GHz [35]. The MPC channel parameters and transmit performance results using a cluster model were derived and analyzed. In [36], indoor channel measurements were conducted at 13–17 GHz bands by using a VNA and a 20×20-element virtual uniform rectangular array (URA). The variations of channel parameters such as narrowband channel gain, K-factor, and RMS DS over the array were investigated. These measurements and analysis are relatively few and not sufficient to fully characterize the mmWave massive MIMO channels, and more comprehensive massive MIMO channel measurements should be conducted at mmWave bands.

To fill the aforementioned gaps, we carry out massive MIMO channel measurements at 11, 16, 28, and 38 GHz bands in indoor office environments by using a VNA and large virtual URAs. The main contributions and novelties of this paper are summarized as follows:

1) This paper compares the propagation characteristics of different mmWave frequency bands. The 11, 16, 28, and 38 GHz channel measurements are carried out with the same configuration. The measurement data are processed with the SAGE algorithm. Temporal-spatial channel characteristics like average power delay profile (APDP), power azimuth profile (PAP), power elevation profile (PEP), RMS DS, azimuth angular spread (AAS), elevation angular spread (EAS), and their cumulative distribution functions (CDFs) and correlation properties are obtained and compared.
2) New massive MIMO properties are validated for mmWave bands. Especially, spherical wavefront, cluster birth-death, and non-stationarity over antenna array axis are validated for the four mmWave bands by investigating variations of temporal-spatial channel characteristics

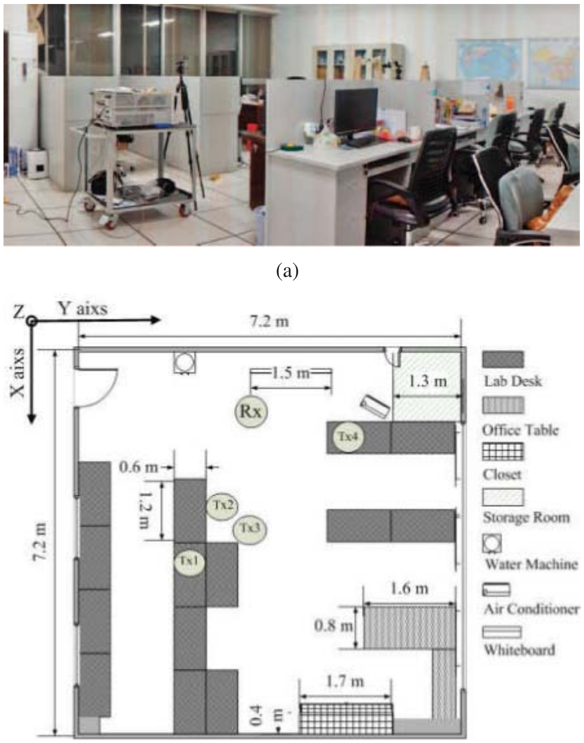

(a)

(b)

Fig. 1. (a) Photo of the office environment and (b) layout of the office.

including PDP, PAP, PEP, RMS DS, AAS, and EAS.

3) Wideband channel capacities are evaluated for mmWave massive MIMO channels at different frequency bands.
4) The propagation graph (PG) model and geometry based stochastic model (GBSM) are applied to verify the measurements.

The remainder of this paper is organized as follows. Section II describes the measurement environment, measurement system setup, and channel measurements. In Section III, the SAGE algorithm and post-processing methods are presented. The comparison of channel characteristics at different mmWave bands, validation of new massive MIMO properties, channel capacities, and channel models are described and analyzed in Section IV. Finally, conclusions are drawn in Section V.

## II. mmWAVE MASSIVE MIMO CHANNEL MEASUREMENTS

### A. Measurement Environment

The channel measurements are conducted in an indoor office environment with room size of 7.2×7.2×3 $m^3$, as shown in Fig. 1(a) [37]. The office is furnished with multiple chairs, desks, and a table. The desks are about 0.75 m high at desktop level but with an additional vertical clapboard having about 0.45 m height. Thus, the total height is about 1.2 m. In addition, the desks and table are equipped with several computers and electronic devices. Other large objects include a closet, an air conditioner, a water machine, and a whiteboard. The layout and sizes of main objects in the office are shown in Fig. 1(b). The height of the closet is about 2.4 m. The walls, floor and ceiling are made of concrete. Parts of the floor and ceiling are made of anti-static-electricity board. There are several windows on both sides of the wall.

### B. Measurement System Setup

The channel sounder consists of a Keysight N5227A VNA, a series of standard gain horn antennas, a biconical antenna, an antenna positioner, cables, connectors, a tripod, and a laptop. The measurement system is auto-controlled by the laptop with programs. The laptop controls not only the VNA with standard commands for programmable instruments (SCPI) but also the antenna positioner with C# language. The programs are then integrated into MATLAB. The customized high accuracy and high speed antenna positioner can scan in X and Y axes in the area of 60×60 $\text{cm}^2$. The VNA can sweep over large self-defined frequency bandwidths within a short time. The intermediate frequency (IF) filter bandwidth is set to 500 Hz to reduce the power level of the noise floor. In channel measurements, the phase-stable low loss cables were used to connect the Tx and Rx antennas to the VNA. Port 1 of the VNA sends the transmitted frequency sweeping signal and is connected to the Tx antenna, while Port 2 receives the fading signal and is connected to the Rx antenna. The VNA can measure and save the scattering parameters. The $S_{21}$ parameter is the channel transfer function (CTF) between Tx and Rx, and the channel impulse response (CIR) can be obtained by the inverse Fourier transform with a window function. The antenna locations are shown in Fig. 1(b). The coordinate of the Rx antenna is (1, 3, 1.45), and the coordinates of Tx1–Tx4 are (4, 2.2, 2.6), (3.2, 2.4, 2.6), (3.6, 3, 2.6), and (2, 5.2, 2.6), respectively. The Tx and Rx were used to mimic the user equipment (UE) and access point (AP), respectively. The Rx antenna was placed at the open space of the room, while the four Tx antenna positions were chosen to keep the Tx–Rx distances in the order of 3 m for observing the near field effect in massive MIMO channel measurements. As a single horn antenna cannot cover the whole 10–40 GHz frequency bands, at the Tx side, four standard gain vertical polarized horn antennas working at 10–15, 15–22, 22–33, and 33–50 GHz bands are used to measure 11, 16, 28, and 38 GHz bands, respectively. Different types of connectors are used to connect antennas and cables. For each frequency band, the antenna gain is the same 10 dBi with a half power beamwidth (HPBW) of 55° to cover a large space. The Rx antenna is a vertical polarized biconical antenna working at 3–40 GHz bands with gain of 3 dBi. Its radiation pattern is omni-directional for the whole bands. During the measurement, the Tx antenna was aligned to the center of the Rx large antenna array and placed on a tripod at four locations, while the Rx antenna was placed on an antenna positioner to shift positions to form a large virtual URA. The measurements are conducted automatically with the environment being kept quasi-static. At first, Port 1 of the VNA is triggered and swept in the defined frequency bands, and the fading signal in the environment is received by Port 2. After the CTF is obtained and saved, the Rx antenna moves to the next defined position, and the VNA begins to measure the channel again. To scan in the large URA efficiently, the Rx antenna moves in the

TABLE II
MEASUREMENT SYSTEM SETUP

| Center frequency (GHz) | 11 | 16 | 28 | 38 |
|---|---|---|---|---|
| Wavelength (mm) | 27 | 19 | 11 | 8 |
| Bandwidth (GHz) | 2 | 2 | 4 | 4 |
| Delay resolution (ns) | 0.5 | 0.5 | 0.25 | 0.25 |
| Output power (dBm) | 15 | 15 | 13 | 8 |
| Sweeping points | 401 | 401 | 801 | 801 |

TABLE III
ANTENNA ARRAY CONFIGURATION

| Center frequency (GHz) | 11 | 16 | 28 | 38 |
|---|---|---|---|---|
| Spacing step (mm) | 12 | 8 | 4 | 3 |
| Array size ($\text{cm}^2$) | 60×60 | 60×60 | 36×36 | 36×36 |
| Array elements | 51×51 | 76×76 | 91×91 | 121×121 |
| Sub-array elements | 10×10 | 15×15 | 15×15 | 20×20 |
| Sliding window | 1:2:41 | 1:3:61 | 1:3:76 | 1:2:101 |
| Rayleigh distance (m) | 1.7 | 2.7 | 1.2 | 1.6 |

X–Y plane with an S-shape. Due to the large number of antenna positions, the whole measurement time for one frequency band can be several hours. Before the measurement at each Tx antenna location, a back-to-back calibration is conducted by connecting the cables directly to remove the responses of the measurement system and cables for each frequency band.

The measurement system setup for the four bands is shown in Table II, while the antenna array configuration is shown in Table III. For 11 and 16 GHz lower bands, the signal bandwidth is 2 GHz, the delay resolution is 0.5 ns, and the array size is 60×60 $\text{cm}^2$. For 28 and 38 GHz higher bands, the signal bandwidth is 4 GHz, the delay resolution is 0.25 ns, and the array size is 36×36 $\text{cm}^2$. The frequency resolution for the four bands is 5 MHz. The spacing steps for the four bands are 12, 8, 4, and 3 mm, which are within half-wavelength and about 0.44, 0.43, 0.37, and 0.38, respectively, when normalized to the corresponding wavelengths. Thus, the array elements for the four bands are 51×51, 76×76, 91×91, and 121×121, respectively.

The radiation field of antennas is usually divided into the near field region (Fresnel zone) and far field region (Fraunhofer zone), which are defined by the Rayleigh distance $R = \frac{2D^2}{\lambda}$. Here, $\lambda$ is the wavelength and $D$ in general can be taken as the maximum dimension of the antenna. For $N \times N$-element URA with a spacing step $d$, $D$ is taken as $\sqrt{2}(N-1)d$. Then, the Rayleigh distance $R$ is given as $4d^2(N-1)^2/\lambda$. For large antenna arrays, the Rayleigh distance can be very large and the far field assumption can easily be violated. To apply the SAGE algorithm, the large antenna array is divided into several sub-arrays and a sliding window is used over the array on Y axis. The sub-array antenna elements for the four bands are 10×10, 15×15, 15×15, and 20×20, respectively, and the calculated sub-array Rayleigh distances are within the Tx–Rx distances, which can fulfill the far field and plane wavefront assumptions.

## III. MEASUREMENT DATA PROCESSING METHODS

For VNA-based channel measurements, due to the quasi-static nature of the environment and relatively long measurement time, a large number of snapshots are not available. In reality, there is only a single snapshot. Thus, conventional subspace based high resolution algorithms like multiple signal classification (MUSIC) and estimation of signal parameters via rotational invariance technique (ESPRIT) cannot be used because they rely on an estimation of the noise covariance matrix which is rank deficient in the single-snapshot scenario. The maximum likelihood (ML) based SAGE algorithm [38], [39] is applied to the data post-processing instead.

The high-resolution SAGE algorithm is widely used for wireless channel parameter estimations. The algorithm can jointly estimate the complex amplitude, delay, azimuth angle, and elevation angle of the MPCs. The received signal $\mathbf{y}(t)$ is assumed to consist of a finite number $L$ of specular plane waves, i.e.,

$$\mathbf{y}(t) = \sum_{l=1}^{L} \mathbf{s}(t; \boldsymbol{\Theta}_l) + \sqrt{\frac{N_0}{2}} \mathbf{N}(t) \tag{1}$$

$$\mathbf{s}(t; \boldsymbol{\Theta}_l) = \alpha_l \mathbf{c}(\boldsymbol{\Omega}_l) u(t - \tau_l) \tag{2}$$

$$\mathbf{c}(\boldsymbol{\Omega}_l) \triangleq [c_1(\boldsymbol{\Omega}_l), \ldots, c_{N^2}(\boldsymbol{\Omega}_l)]^T \tag{3}$$

$$c_n(\boldsymbol{\Omega}_l) = \exp(\mathrm{j}2\pi\lambda^{-1}\langle e(\boldsymbol{\Omega}_l), r_n\rangle), n = 1, \ldots, N^2 \tag{4}$$

$$\begin{aligned}\langle e(\boldsymbol{\Omega}_l), r_n\rangle &= [x_n, y_n, z_n] \\ &\quad \times [\cos(\phi_l)\sin(\theta_l), \sin(\phi_l)\sin(\theta_l), \cos(\theta_l)]^{\mathrm{T}}\end{aligned} \tag{5}$$

where $u(t)$ is the transmitted signal, $\mathbf{s}(t; \boldsymbol{\Theta}_l)$ is the $l$th MPC, $\mathbf{N}(t)$ is the standard $N^2 \times 1$-dimensional complex white Gaussian noise with spectral height of $N_0$, $\mathbf{c}(\boldsymbol{\Omega}_l)$ is the steering vector of the Rx array, $c_n(\boldsymbol{\Omega}_l)$ is the steering vector of the $n$th antenna array, and $r_n$ denotes the $n$th antenna array element with coordinates of $x_n$, $y_n$, and $z_n$. The parameter sets to be estimated are $\boldsymbol{\Theta}_l = [\alpha_l, \tau_l, \phi_l, \theta_l], l = 1, ..., L$, where $\alpha_l$, $\tau_l$, $\phi_l$, and $\theta_l$ denote the complex amplitude, delay, azimuth angle, and elevation angle for the $l$th MPC, respectively.

The coordinate-wise iteration to obtain the estimate $\widehat{\boldsymbol{\Theta}}_l^{''}$ given the previous estimate $\widehat{\boldsymbol{\Theta}}_l^{'}$, is given as

$$\widehat{\tau}_l^{''} = \arg\max_{\tau}\{|\mathrm{z}(\tau, \widehat{\boldsymbol{\Omega}}_l^{'}; \hat{\mathbf{x}}_l(t; \hat{\boldsymbol{\Theta}}_l^{'}))|\} \tag{6}$$

$$\widehat{\boldsymbol{\Omega}}_l^{''} = [\widehat{\phi}_l^{''}, \widehat{\theta}_l^{''}] = \arg\max_{\boldsymbol{\Omega}}\{|\mathrm{z}(\hat{\tau}_l^{''}, \boldsymbol{\Omega}; \hat{\mathbf{x}}_l(t; \hat{\boldsymbol{\Theta}}_l^{'}))|\} \tag{7}$$

$$\widehat{\alpha}_l^{''} = \frac{1}{N^2}\mathrm{z}(\hat{\tau}_l^{''}, \hat{\boldsymbol{\Omega}}_l^{''}; \hat{\mathbf{x}}_l(t; \hat{\boldsymbol{\Theta}}_l^{'})). \tag{8}$$

The cost function reads as

$$\mathrm{z}(\tau, \boldsymbol{\Omega}; \hat{\mathbf{x}}_l(t; \hat{\boldsymbol{\Theta}}_l^{'})) \triangleq \mathbf{c}^H(\boldsymbol{\Omega}) \int u(t' - \tau)\hat{\mathbf{x}}_l(t'; \hat{\boldsymbol{\Theta}}_l^{'}))dt' \tag{9}$$

$$\hat{\mathbf{x}}_l(t; \hat{\boldsymbol{\Theta}}_l^{'}) \triangleq \mathbf{y}(t) - \sum_{l'=1, l' \neq l}^{L} \mathbf{s}(t; \hat{\boldsymbol{\Theta}}_{l'}^{'}) \tag{10}$$

where $()^{\mathrm{H}}$ is the conjugate transpose operator.

After some iterations, the estimated parameters will converge to stable values.

In the SAGE algorithm, the number of MPCs $L$ is usually predefined large enough to capture all significant paths. Some values for the numbers of MPCs have been investigated. We found that when the number of MPCs equals 100, a good trade-off between accuracy and computational complexity can be achieved. This number was also used in [13] for LOS propagation scenarios. The delay resolution is the same with the measurement data, while the angle resolution is 1°. The estimated spatial-temporal MPC parameters are used to obtain some important propagation channel characteristics.

The CTF matrix $\mathbf{H}(n,k) \in C^{N^2 \times K}$ can be obtained by synthesizing the estimated MPCs, i.e.,

$$\mathbf{H}(n,k) = \sum_{l=1}^{L} \alpha_l \exp(j2\pi\lambda^{-1}\langle e(\Omega_l), r_n\rangle)\exp(-j2\pi f_k \tau_l) \quad (11)$$

where $f_k$ is the $k$th frequency point and $K$ is the number of sweeping points.

The CIR can be obtained by the inverse Fourier transform of $\mathbf{H}(n,k)$, i.e.,

$$h(n,:) = IFFT(\mathbf{H}(n, 1:K)), n = 1, ..., N^2. \quad (12)$$

The PDP is the square of the amplitude of the CIR, i.e.,

$$PDP = |h(n,k)|^2. \quad (13)$$

For the measurement and estimated data, the APDP is obtained by averaging PDPs over the array,

$$APDP = \frac{1}{N^2}\sum_{n=1}^{N^2} |h(n,k)|^2. \quad (14)$$

The PAP and PEP can be obtained as

$$PAP = \sum_{l=1}^{L} |\alpha_l|^2 \delta(\phi - \phi_l) \quad (15)$$

$$PEP = \sum_{l=1}^{L} |\alpha_l|^2 \delta(\theta - \theta_l) \quad (16)$$

where $\delta()$ is the Dirac delta function. Note that the power of estimated MPCs with the same azimuth or elevation angles are summed up to get a unique power value.

The RMS DS is an important second-order statistic to describe the dispersion of the PDP and can be calculated as

$$\tau_{rms} = \sqrt{\frac{\sum_1^L |\alpha_l|^2 \tau_l^2}{\sum_1^L |\alpha_l|^2} - \left(\frac{\sum_1^L |\alpha_l|^2 \tau_l}{\sum_1^L |\alpha_l|^2}\right)^2}. \quad (17)$$

Similarly, the RMS angle spread (AS) is an important second-order statistic to describe the dispersion of the power angular profile and can be calculated as

$$\psi_{rms} = \sqrt{\frac{\sum_1^L |\alpha_l|^2 \psi_l^2}{\sum_1^L |\alpha_l|^2} - \left(\frac{\sum_1^L |\alpha_l|^2 \psi_l}{\sum_1^L |\alpha_l|^2}\right)^2} \quad (18)$$

where $\psi_l$ denotes the azimuth angle $\phi_l$ or elevation angle $\theta_l$, and $\psi_{rms}$ denotes RMS AAS $\phi_{rms}$ or RMS EAS $\theta_{rms}$.

The correlation coefficient between the $m$th CIR $h_m$ and $n$th CIR $h_n$ is defined as

$$\rho_{h_m,h_n} = \frac{E\left\{(h_m - \bar{h}_m)(h_n - \bar{h}_n)\right\}}{\sqrt{E\left\{(h_m - \bar{h}_m)^2(h_n - \bar{h}_n)^2\right\}}} \quad (19)$$

where $\bar{h}_m$ and $\bar{h}_n$ are the mean values of CIRs, and $E\{\}$ is the expectation operation. As the distance between the $m$th and $n$th antenna element increases, the correlation coefficient will decrease.

TABLE IV

POWER DECAY RATE FOR DIFFERENT BANDS

| Power decay rate (dB/ns) | 11 GHz | 16 GHz | 28 GHz | 38 GHz |
|---|---|---|---|---|
| Tx1 | 0.33 | 0.22 | 0.29 | 0.32 |
| Tx2 | 0.45 | 0.37 | 0.40 | 0.52 |
| Tx3 | 0.29 | 0.29 | 0.33 | 0.34 |
| Tx4 | 0.63 | 0.55 | 0.26 | 0.42 |

## IV. mmWAVE MASSIVE MIMO CHANNEL MEASUREMENT RESULTS AND ANALYSIS

### *A. Comparison of Different* mm*Wave Bands*

*1) APDP Results:* For each frequency band and each Tx location, the sub-array measurement data are processed with the SAGE algorithm. As an example, the measured and estimated APDPs for the four bands at Tx2 location are shown in Fig. 2. The APDPs are obtained for the center sub-array of the large URA. For each frequency band, the estimated results match well with the measured data. Most of the MPCs are extracted accurately, except that some weak paths with large delays are not extracted. A strong LOS path is observed with the same delay but different power gains. The relative received power of the LOS path are −59.0, −62.8, −67.2, and −71.7 dB, respectively. The attenuation tends to be larger as the frequency increases. The reflected and scattered MPCs show similar delay distributions. But some differences are also observed. For example, a MPC with delay of 40 ns is only observed at 11 GHz, while two MPCs with delay of 33 ns and 50 ns are not observed at 11 GHz. The maximum excess delay for the four bands is within 70 ns. As the office is small, a delay of 60 ns which is equal to 18 m distance may be caused by second-order reflection. Table IV shows the power decay rate for the four bands. In line with observations in [18], the main differences between the four bands lie in power levels of MPCs and the power decay rate. By using the time cluster algorithm in [41] with recommended minimum inter-cluster void interval of 5 ns for indoor scenarios, an average of seven time clusters of MPCs are obtained for the four bands.

*2) PAP and PEP Results:* The PAPs and PEPs are related with the measurement environments and antenna locations. Fig. 3 shows the PAPs at four Tx locations. The azimuth angles show similar properties for different frequency bands at the same Tx location. For each frequency band, the LOS path arrives with azimuth angle of −17°, −16°, 0°, and 70° at the four Tx locations, respectively. By using the spatial lobe algorithm in [41] with 30 dB power threshold with respect to the maximum peak power, an average of four spatial lobes of MPCs are obtained for the four bands. Because height differences between Tx and Rx antennas are the same for the four Tx locations, and the Tx–Rx distances on horizontal plane are close, the elevation angles show almost the same properties for different Tx locations. As an example, PEPs at Tx1 location is shown in Fig. 4. The elevation angles is in the range of 30°–150°. The LOS path arrives with angle about 70°, which is an approximate of $\arccos(\frac{2.6-1.45}{3.3})$, for all frequency bands at each Tx location. To verify the azimuth angle estimation results, the PAPs for the Rx side are plotted in the environment layout at each Tx location, as shown in Fig. 5.

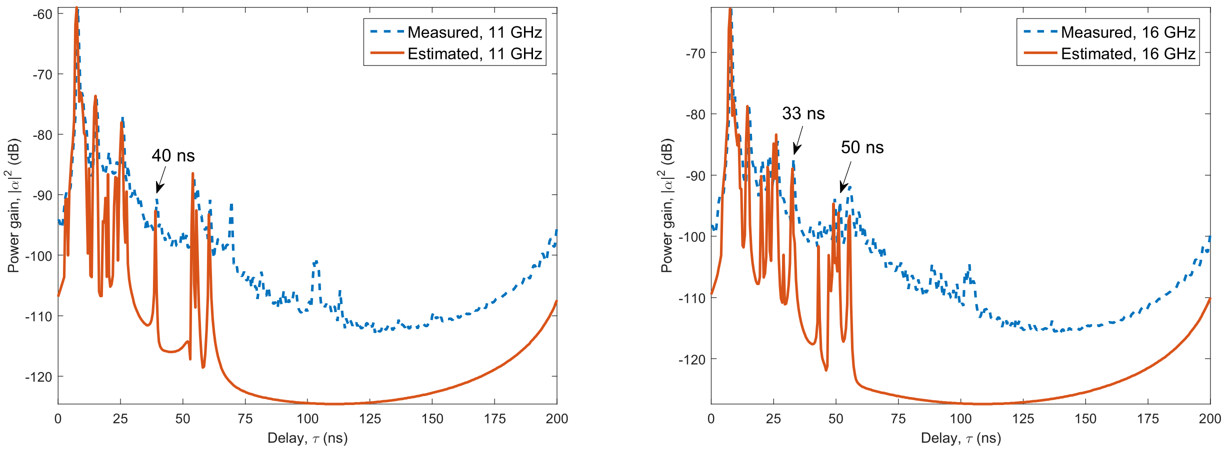

(a) Measured and estimated APDPs at 11 GHz.

(b) Measured and estimated APDPs at 16 GHz.

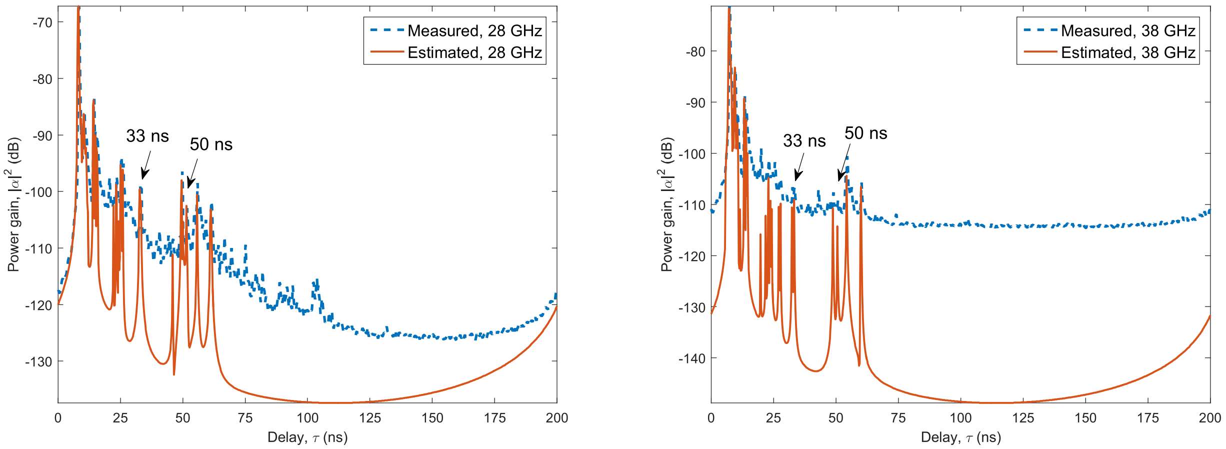

(c) Measured and estimated APDPs at 28 GHz.

(d) Measured and estimated APDPs at 38 GHz.

Fig. 2. (a) Measured and estimated APDPs at 11 GHz; (b) Measured and estimated APDPs at 16 GHz; (c) Measured and estimated APDPs at 28 GHz; (d) Measured and estimated APDPs at 38 GHz.

For each Tx location, the LOS direction is pointed to the Rx antenna location, while other reflection MPCs can correspond with scatterers in the environment according to the delay and angle information of MPCs.

*3) RMS DS and AS:* The RMS DS and AS are important second-order statistics to characterize the channel dispersion in delay and angular domains. The RMS DS is related with channel coherence bandwidth and inter-symbol interference, while the RMS AS is related to the directivity of MPCs. Fig. 6 shows cumulative distribution functions (CDFs) of RMS DS, AAS, and EAS for the four bands over the four Tx locations. The RMS DS, AAS, and EAS are in the range of 5–15 ns, 20°–100°, and 15°–35°, respectively. All the measured data are fitted by a Gaussian Normal distribution $N(\mu, \sigma^2)$, where $\mu$ and $\sigma$ are the mean value and standard deviation of random variables. The distribution parameters are shown in Table V. We can see that 38 GHz channel tends to have the smallest DS, AAS, and EAS. The DS at 28 GHz tends to be larger than other bands. For EAS, the 11 GHz band tends to be the largest one. The fitted mean values of DS and EAS are close for the four bands, while the 38 GHz bands shows the smallest mean value of AAS.

TABLE V

PARAMETERS FOR NORMAL DISTRIBUTIONS

| Fitting parameters | DS | AAS | EAS |
|---|---|---|---|
| 11 GHz | $N(9.1,2.3^2)$ | $N(65.6,7.3^2)$ | $N(27.9,2.7^2)$ |
| 16 GHz | $N(10.2,2.9^2)$ | $N(67.4,12.7^2)$ | $N(25.5,4.5^2)$ |
| 28 GHz | $N(10.6,2.6^2)$ | $N(64.6,16.5^2)$ | $N(24.3,3.6^2)$ |
| 38 GHz | $N(8.5,2.0^2)$ | $N(49.8,22.2^2)$ | $N(23.8,3.4^2)$ |

*4) Correlation Properties:* Fig. 7 shows the CIR correlation coefficients between the first antenna position and the $n$th antenna over the array on Y axis. The correlation distance can be defined as the distance when the correlation coefficient is equal to 0.5. We can see that the correlation coefficients are mainly affected by the Tx antenna location. Tx4 has the largest correlation coefficients. Tx2 and Tx3 show similar correlation coefficients. Compared with 28 and 38 GHz higher bands, in 11 and 16 GHz lower bands, the spacing steps are larger and the correlation coefficients tend to decrease slower. The total distances of the measured array on Y axis for 11, 16, 28, and 38 GHz bands are about 22, 32, 33, and 45, respectively, when they are normalized to the corresponding wavelengths. Table VI shows the calculated correlation distances.

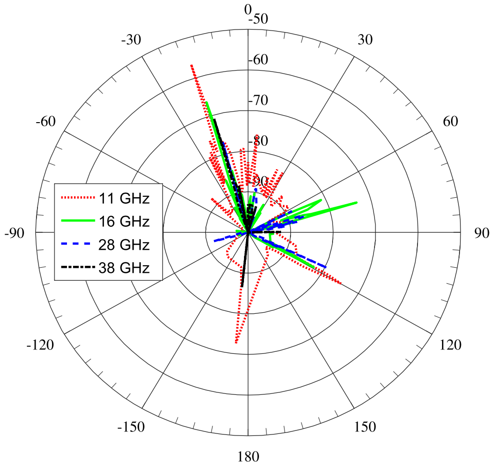

(a) PAPs at Tx1.

(b) PAPs at Tx2.

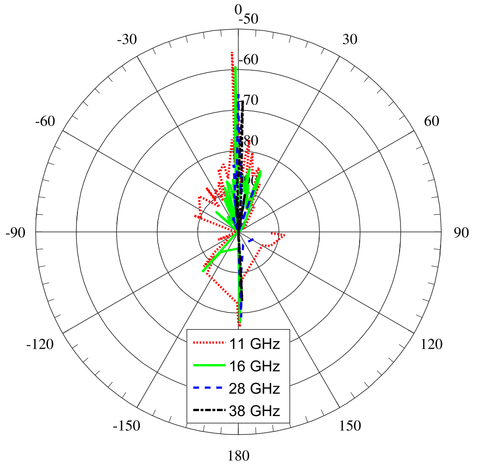

(c) PAPs at Tx3.

(d) PAPs at Tx4.

Fig. 3. (a) PAPs at Tx1; (b) PAPs at Tx2; (c) PAPs at Tx3; (d) PAPs at Tx4.

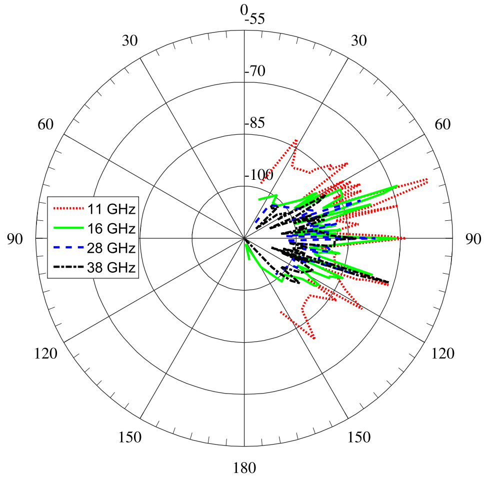

Fig. 4. PEPs at Tx1.

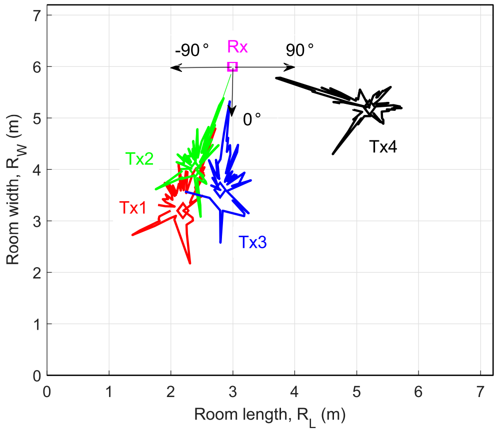

Fig. 5. PAPs validation for the measurement environment.

The correlation distances range between 0.11 m and 0.47 m are observed for all frequency bands and Tx locations.

### *B. Massive MIMO Properties*

*1) Spherical Wavefront Property:* Under far field or plane wavefront assumption, the electromagnetic waves propagate parallel to each other, thus the arrival angles of MPCs will be the same for all antenna elements [42]. As the number of

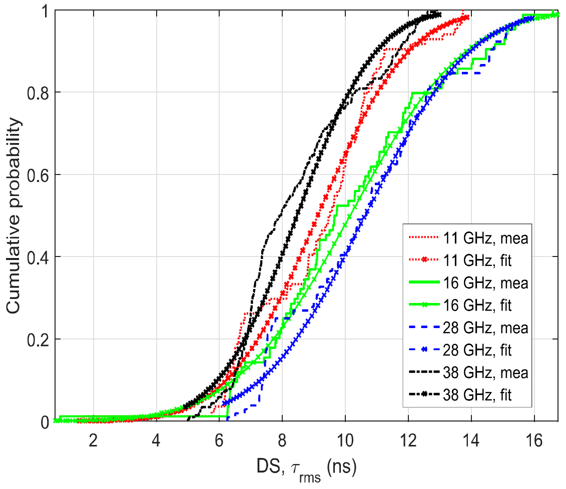

(a) CDF of DS

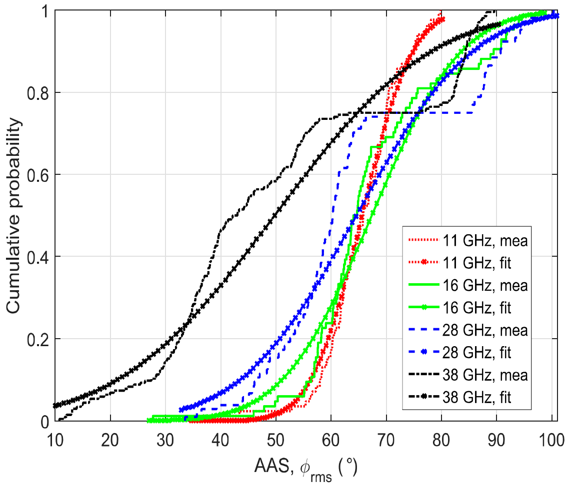

(b) CDF of AAS

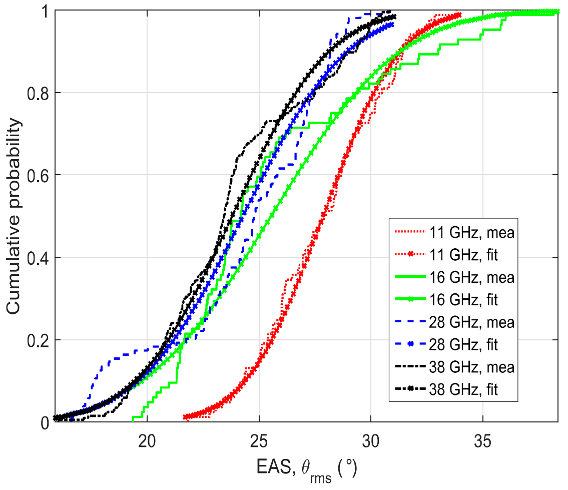

(c) CDF of EAS

Fig. 6. (a) CDF of DS; (b) CDF of AAS; (c) CDF of EAS.

TABLE VI

CORRELATION DISTANCE FOR DIFFERENT BANDS

| Correlation distance (m) | 11 GHz | 16 GHz | 28 GHz | 38 GHz |
|---|---|---|---|---|
| Tx1 | 0.22 | 0.1 | 0.07 | 0.11 |
| Tx2 | 0.17 | 0.14 | 0.11 | 0.13 |
| Tx3 | 0.17 | 0.18 | 0.12 | 0.12 |
| Tx4 | 0.47 | 0.46 | 0.24 | 0.35 |

antennas increases to hundreds, the aperture of the antenna array becomes much larger. The Tx–Rx may be within the Rayleigh distance, and the far field or plane wavefront may be violated. Because the SAGE algorithm is based on plane wavefront assumption, it is impossible to process the large antenna array measurement data. To deal with the problem, the large array is divided into several sub-arrays. For each sub-array, the calculated Rayleigh distance is smaller than the Tx–Rx distance, and the SAGE algorithm is applied. A sliding window is used over the array on Y axis. As the sub-array slides over the array on Y axis, the estimated channel parameters will variate gradually over the array. Fig. 8 shows the LOS path azimuth angle variations for the four bands over the array at the four Tx locations. Because Tx1 and Tx2 are at the left side of the room, as the window slides from left to right, the LOS azimuth angle shifts from $-12°$ to $-22°$ and from $-10°$ to $-24°$, respectively. Tx3 is at the middle of the room, so the LOS azimuth angle shifts from $5°$ to $-8°$. As Tx4 is at the right side of the room, the LOS azimuth angle shifts from $73°$ to $68°$. Because the array size of 28 GHz and 38 GHz is smaller, the LOS azimuth angle shifts in a smaller range, but the angle shift rate are similar for different frequency bands. The rates of azimuth angle drift are about $23°/m$, $29°/m$, $27°/m$, and $10°/m$ for the four Tx locations, respectively. These angle drifts can be verified by using simple triangular geometry relationships given the Tx and Rx settings. As the Tx–Rx distances are in the order of 3 m with the same antenna height differences for the four Tx locations, the LOS elevation angles at the four Tx locations show similar characteristics. Fig. 9 shows the LOS elevation angle shifts at Tx4. An angle drift of as large as $10°$ is observed. The step-wise change of the angle is due to the fact that the azimuth and elevation angle resolution of the SAGE algorithm is set as $1°$. All the results indicate that the plane wavefront assumption is not valid and the spherical wavefront should be considered.

*2) Cluster Birth-Death Property:* Certain clusters are not observable over the whole array, and each antenna element on the large array has its own set of clusters. The clusters may appear and disappear over the array axis, which can be described by a Markov birth-death process [43]. Fig. 10 shows the measured PDP variations over the array for 16 GHz band at Tx1 location. The LOS path and strong reflected MPCs have delay drifts over the array, and some MPCs are not observable over the whole array. As a comparison, Fig. 11 shows the estimated PDP variations over the array for 16 GHz band at Tx1 location. Similar results are observed. Fig. 12 and Fig. 13 show the cluster birth-death property of the PAPs and PEPs over the array axis for 16 GHz band at Tx1 location, respectively. The LOS path and some first-order reflection MPCs can be seen over the array, while some MPCs are not observable at each antenna position. The results verify the cluster birth-death property for mmWave bands. As the measurement environment is kept quasi-static, the reason for cluster birth-death may be that as the antenna moves in a large area, the antenna cannot see all the objects in the environment.

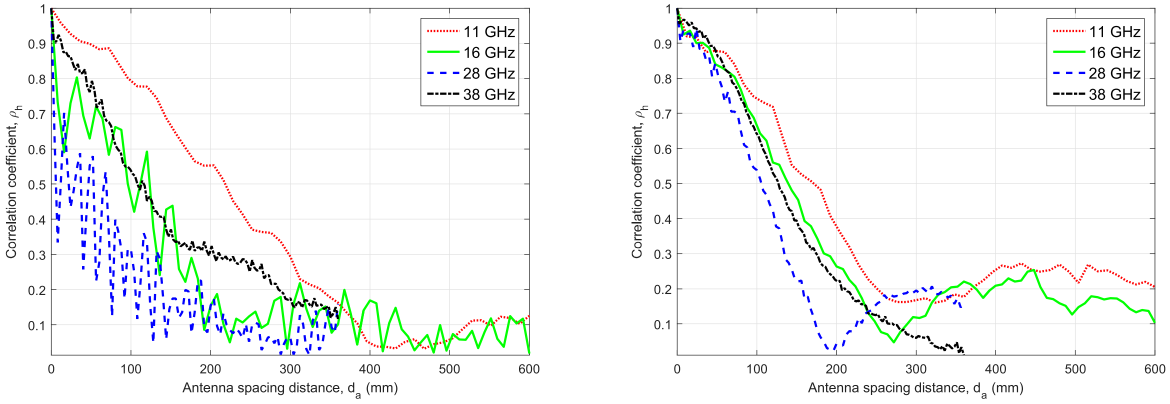

(a) Correlation at Tx1.

(b) Correlation at Tx2.

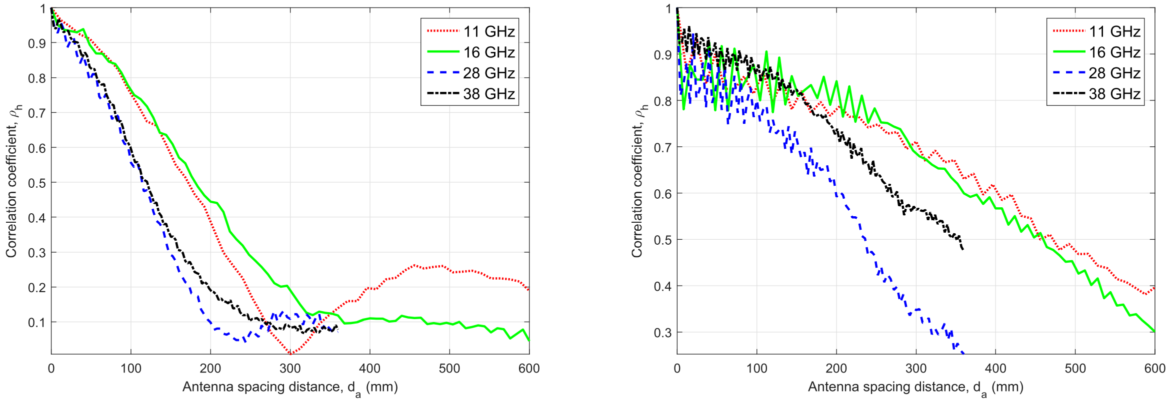

(c) Correlation at Tx3.

(d) Correlation at Tx4.

Fig. 7. (a) Correlation at Tx1; (b) Correlation at Tx2; (c) Correlation at Tx3; (d) Correlation at Tx4.

Thus, some small objects may be observed by the antenna at one position, while these objects may be out of the visible region of the antenna at another position. A more complex environment is more likely to observe the cluster birth-death property obviously.

*3) Non-Stationarity Property:* For massive MIMO systems, the wide sense stationary (WSS) assumption may be violated, and MPC parameters may vary over the large physical array. As an example, the variations of the LOS path received power over the array at Tx2 location is shown in Fig. 14. The LOS path received power can vary several dB over the large array. The variations of temporal-spatial parameters can also be seen in Figs. 11–13. Fig. 15 shows the DS, AAS, and EAS variations over the array at Tx3 location for the four bands, respectively. As shown in Fig. 15(a), the DS can vary in the range of 3 ns over the array. Fig. 15(b) shows that the azimuth AS can vary 20° over the array. Fig. 15(c) shows that the elevation AS variations are in the range of about 5° over the array. All the results indicate that the mmWave massive MIMO channel shows the non-stationarity property over the array and should not be seen as a WSS channel.

### *C. Channel Capacity*

Channel capacity is the tight upper bound on the rate at which information can be reliably transmitted over a communications channel. For a wideband frequency-selective channel, the channel capacity can be obtained from the measured channel frequency response by [40]

$$C = \frac{1}{K}\sum_{k=1}^{K}\log_2(1+\rho H(f_k)H^{\mathrm{H}}(f_k))(bps/Hz) \qquad (20)$$

where $\rho$ is the signal-to-noise ratio (SNR), $H(f_k)$ is the measured frequency response of the $k$th frequency point.

For the measured channel, the channel frequency response contains the large scale path loss, the attenuation caused by cables and measurement system is calibrated out, so the SNR is calculated as

$$\rho = P + G_t + G_r - N_0 B - NF \qquad (21)$$

where $P$ is the output power of VNA as shown in Table II, $G_t$ and $G_r$ are the gains of Tx and Rx antennas, $N_0$ is the thermal noise power density and assumed to be $-174$ dBm/Hz, $B$ is the measured signal bandwidth, $NF$ is the noise floor of the receiver and assumed to be 8 dB.

The real transmission data rate can be calculated as

$$R = B\log_2(1+\rho - PL)(bps) \qquad (22)$$

where $PL$ is the large scale path loss which can be obtained by averaging the channel frequency response.

Due to the large bandwidth and multi-antennas, mmWave massive MIMO channel will achieve high channel capacity. To have a fair comparison of the channel capacity of different

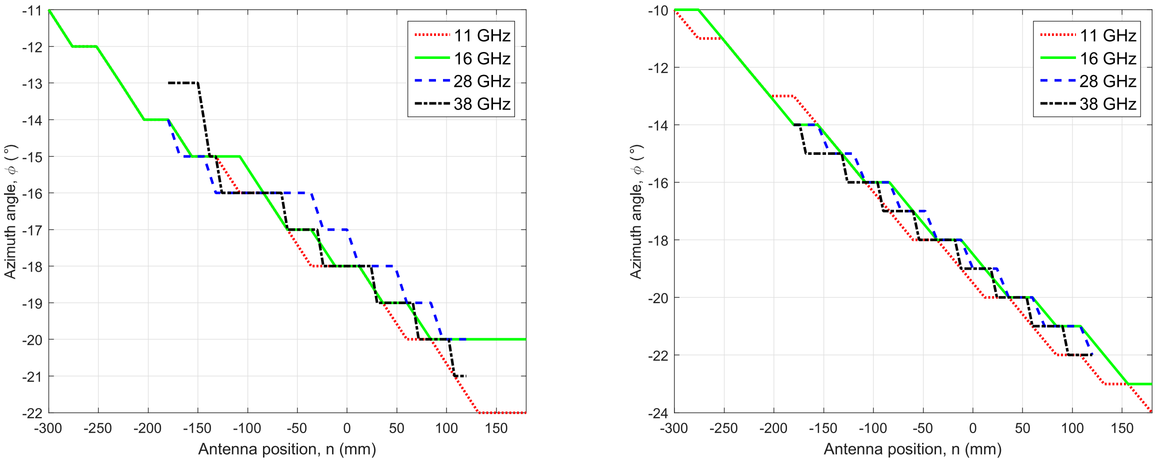

(a) Azimuth angle variations at Tx1

(b) Azimuth angle variations at Tx2

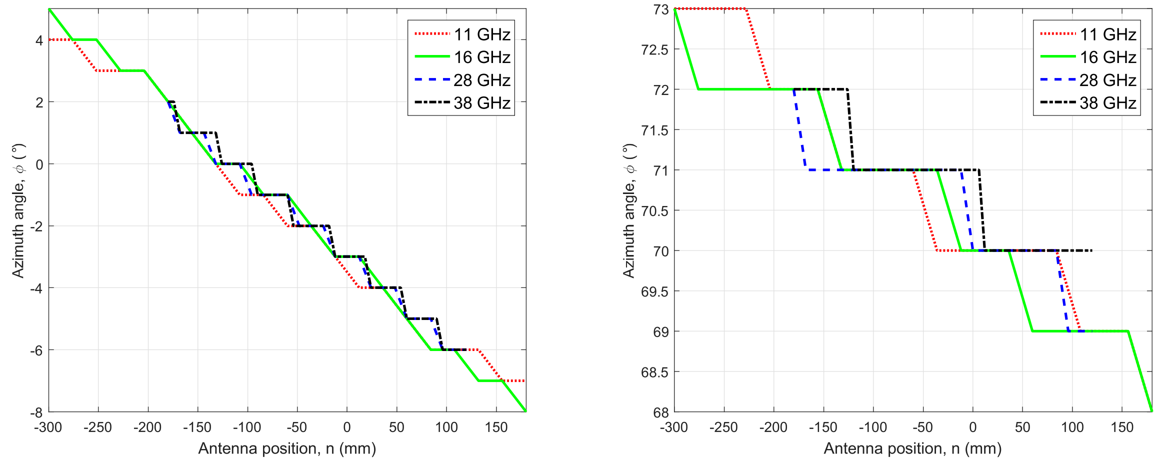

(c) Azimuth angle variations at Tx3

(d) Azimuth angle variations at Tx4

Fig. 8. (a) Azimuth angle variations at Tx1; (b) Azimuth angle variations at Tx2; (c) Azimuth angle variations at Tx3; (d) Azimuth angle variations at Tx4.

TABLE VII

CHANNEL CAPACITY FOR DIFFERENT BANDS

| Channel capacity (bps/Hz) | 11 GHz | 16 GHz | 28 GHz | 38 GHz |
|---|---|---|---|---|
| Tx1 | 23.0 | 20.4 | 15.6 | 15.5 |
| Tx2 | 23.1 | 21.8 | 18.5 | 16.4 |
| Tx3 | 23.2 | 22.0 | 18.1 | 15.6 |
| Tx4 | 24.1 | 23.1 | 18.4 | 15.9 |

bands, a 10×10 sub-array at the array center is used to calculate the channel capacity. The results are shown in Table VII. A channel capacity in the range of 15.5–24.1 bps/Hz is obtained. We can see that the channel capacity decreases as the frequency increases. For 11 GHz and 16 GHz bands, the largest channel capacity is obtained at Tx4 location. For 28 GHz and 38 GHz bands, the largest channel capacity is obtained at Tx2 location.

The transmission data rate for a single antenna at the array center is shown in Table VIII. To have a fair comparison, for the higher bands, 2 GHz bandwidth around the carrier frequency was used for the calculation. The transmission data rate ranges in 5.55–7.39 Gbps. As the frequency increases, the transmission data rate tends to decrease.

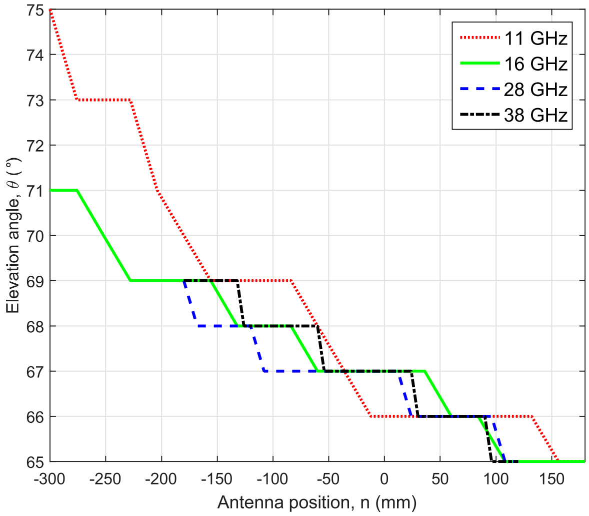

Fig. 9. Elevation angle variations at Tx4.

### *D. Channel Modeling*

*1) PG Model:* In order to model the PDP, a PG based channel modeling approach [44] is used. This model was first proposed in [45] to predict the exponentially decaying PDP

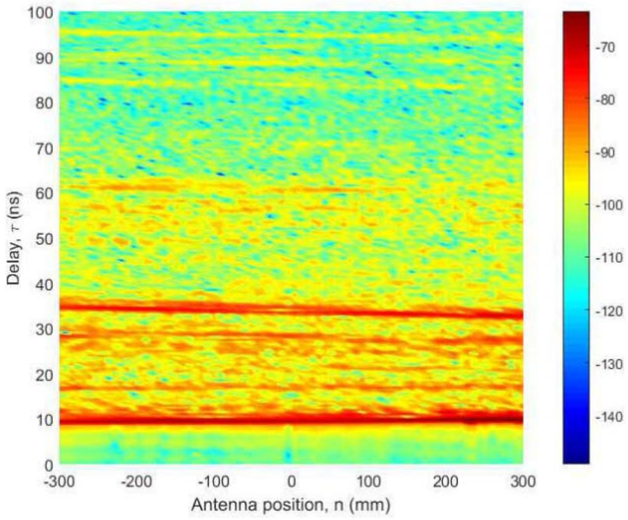

Fig. 10. Measured PDP variations over the array for 16 GHz at Tx1.

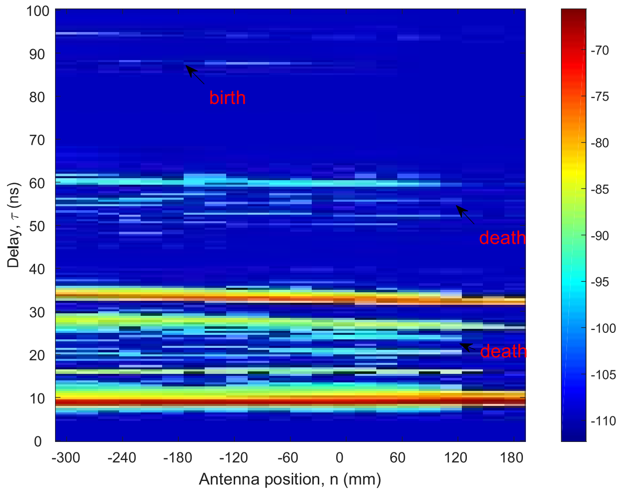

Fig. 11. PDP variations over the array for 16 GHz at Tx1.

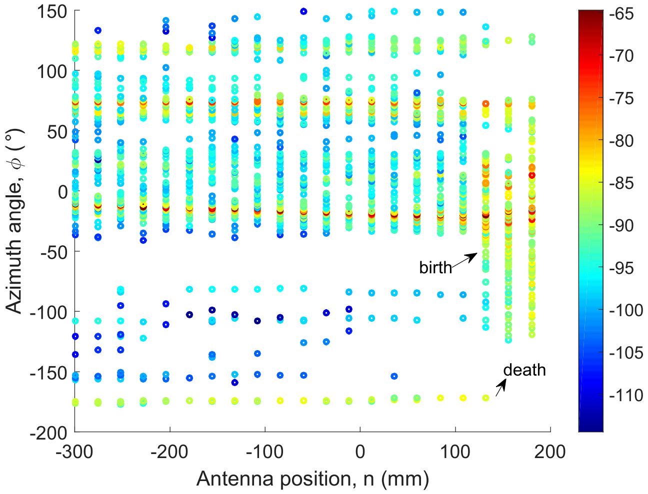

Fig. 12. PAP variations over the array for 16 GHz at Tx1.

which exhibits a transition from specular components at small delays to diffuse components at large delays, especially for ultra wideband systems.

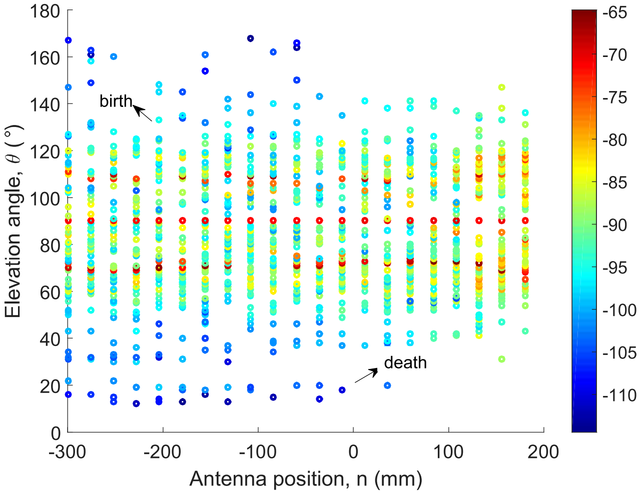

Fig. 13. PEP variations over the array for 16 GHz at Tx1.

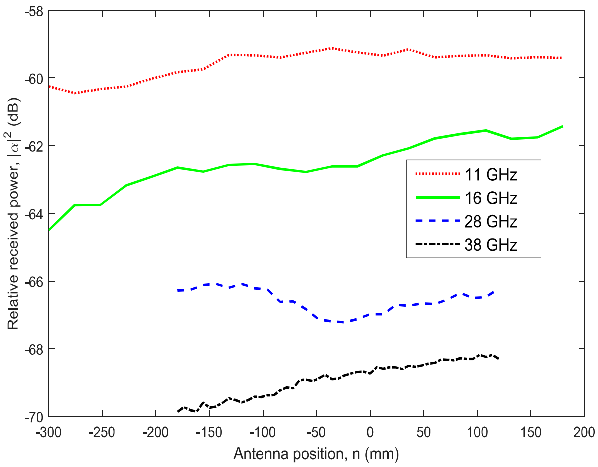

Fig. 14. LOS received power variations at Tx2.

TABLE VIII

TRANSMISSION RATE FOR DIFFERENT BANDS

| Transmission rate (Gbps) | 11 GHz | 16 GHz | 28 GHz | 38 GHz |
|---|---|---|---|---|
| Tx1 | 7.19 | 6.73 | 5.55 | 5.67 |
| Tx2 | 7.22 | 7.00 | 6.52 | 5.99 |
| Tx3 | 7.24 | 7.03 | 6.42 | 5.74 |
| Tx4 | 7.39 | 7.21 | 6.49 | 5.79 |

A directed graph is defined as a pair of disjoint sets of vertices and edges. A propagation graph is a directed graph where vertices represent Txs, Rxs, and scatterers, and edges represent the propagation conditions between the vertices. The connectivity between vertices is described by a probability. The propagation conditions are described by a weighted adjacency matrix of the propagation graph. The generation of weighted adjacency matrix is the same as in [44]. Let us assume that the numbers of Txs, Rxs, and scatterers are $N_t$, $N_r$, and $N_s$, respectively. The weighted adjacency matrix $\mathbf{A}(f) \in C^{(N_t+N_r+N_s)\times\ (N_t+N_r+N_s)}$ takes the form as

$$\mathbf{A}(f) = \begin{bmatrix} \mathbf{0} & \mathbf{0} & \mathbf{0} \\ \mathbf{D}(f) & \mathbf{0} & \mathbf{R}(f) \\ \mathbf{T}(f) & \mathbf{0} & \mathbf{B}(f) \end{bmatrix} \tag{23}$$

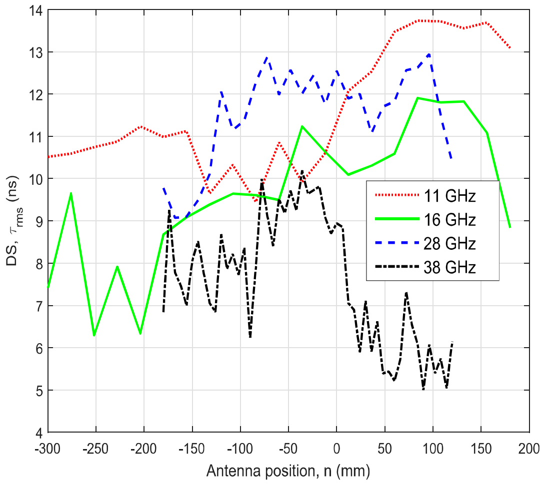

(a) DS variations at Tx3

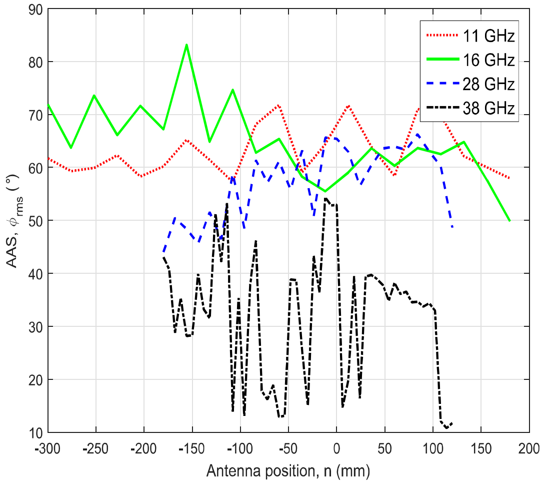

(b) AAS variations at Tx3

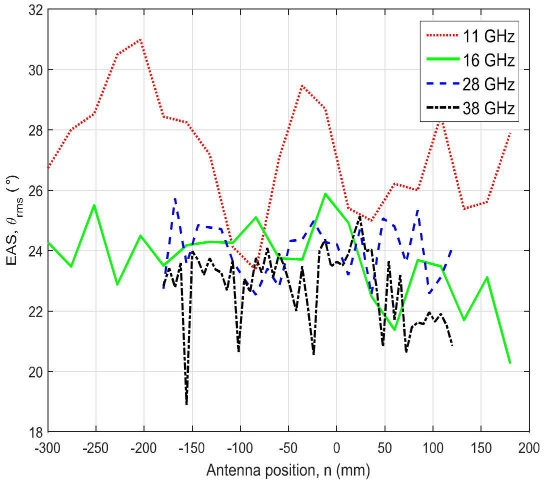

(c) EAS variations at Tx3

Fig. 15. (a) DS variations at Tx3; (b) AAS variations at Tx3; (c) EAS variations at Tx3.

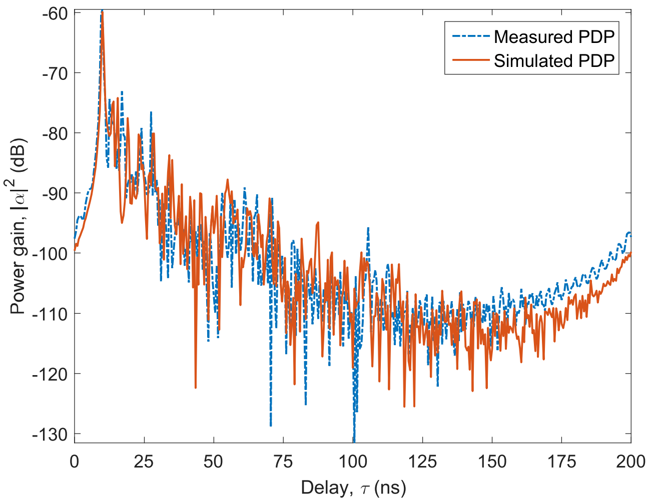

Fig. 16. Comparison of measured and simulated PDPs.

TABLE IX

SIMULATION PARAMETERS FOR CHANNEL MODELING

| Parameters | Values |
|---|---|
| Room size | $7.2\times7.2\times3$ m$^3$ |
| Tx location | (4, 2.2, 2.6) |
| Rx location | $51\times51$, center at (1, 3, 1.45) |
| Number of scatterers | 10 |
| LOS probability | 1 |
| Visibility probability | 0.8 |
| Frequency range | 10–12 GHz |
| Sampling points | 401 |

where $\mathbf{0}$ denotes the all-zero matrix, $\mathbf{D}(f) \in C^{N_r\times N_t}$, $\mathbf{R}(f) \in C^{N_r\times N_s}$, $\mathbf{T}(f) \in C^{N_s\times N_t}$, and $\mathbf{B}(f) \in C^{N_s\times N_s}$ denote the transfer matrices of vertices connecting Txs–Rxs, scatterers–Rxs, Txs–scatterers, and interconnecting scatterers, respectively. The CTF is then read as

$$\mathbf{H}(f) = \mathbf{D}(f) + \mathbf{R}(f)[\mathbf{I} - \mathbf{B}(f)]^{-1}\mathbf{T}(f) \tag{24}$$

where $\mathbf{I}$ is the identity matrix. Given the frequency range and sampling points, the wideband CTF can be obtained. The CIR can then be obtained from it by the inverse Fourier transform.

Unlike a uniform random generation of scatterers in the environment, the extracted delays and angles are used to generate deterministic scatterer positions in the indoor office. As an example, the PDP simulation result of 11 GHz channel at Tx1 is shown and compared with the measurement data in Fig. 16. The simulation parameters are shown in Table IX. As can be seen, the measured and simulated PDPs match well, which verifies the modeling approach for indoor mmWave environments.

*2) GBSM:* The GBSM approach has widely been used for channel modeling [43], [46]. In this paper, we extend the non-stationary wideband twin-cluster massive MIMO model [43] to mmWave bands. The $N_r \times N_t$ channel matrix is $\mathbf{H}(\tau) = \left[h_{qp}(\tau)\right]$ with the entry

$$\begin{aligned} h_{qp}(\tau) = {} & \sqrt{\frac{K_r}{K_r+1}} h_{qp}^{\mathrm{LOS}} \delta\left(\tau - \tau^{\mathrm{LOS}}\right) \\ & + \sqrt{\frac{1}{K_r+1}} \sum_{s=1}^{S} \sum_{m_s=1}^{M_s} h_{qp,s,m_s} \delta\left(\tau - \tau_s - \tau_{m_s}\right) \end{aligned} \tag{25}$$

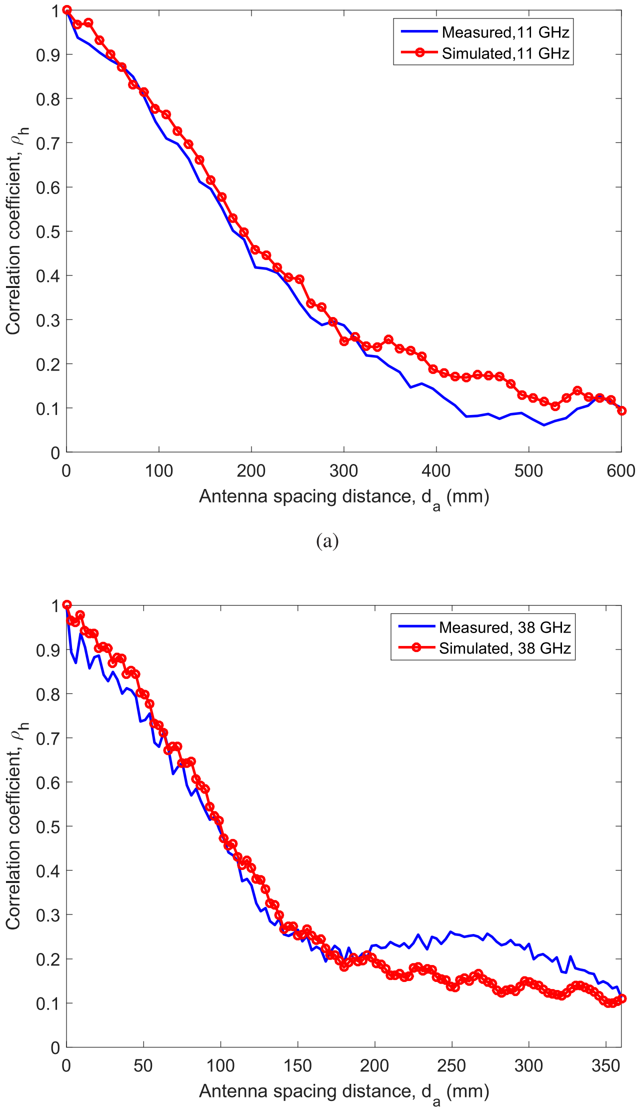

(a)

(b)

Fig. 17. Measured and simulated correlation coefficients for (a) 11 GHz and (b) 38 GHz.

where $K_r$ is the K-factor, $h_{qp}^{\mathrm{LOS}}$ is the amplitude of the LOS path, $\tau^{\mathrm{LOS}}$ is the delay of the LOS path, $S$ is the number of clusters, $M_s$ is the number of rays within the $s$th cluster, $h_{qp,s,m_s}$ is the amplitude of the $m_s$th ray in the $s$th cluster, $\tau_s$ is the delay of the $s$th cluster, and $\tau_{m_s}$ is the relative delay of the $m_s$th ray in the $s$th cluster.

Multiple twin clusters are used to describe different taps of the channel. A twin-cluster is made of the first bounce cluster at the Tx side and the last bounce at the Rx side. The propagation environment between the two clusters are abstracted as a virtual link. The non-stationarity of the channel is modeled by a birth-death process. The number of clusters is assumed to obey a Poisson distribution. The power and delay of rays are generated in a similar way as in the WINNER II channel model. The azimuth and elevation angles are assumed to be Gaussian distributions. Distance vectors are calculated according to the geometry relationships.

To verify the measurement results, the correlation properties simulated by using the GBSM are compared with the measurement results of 11 and 38 GHz at Tx1, as shown in Fig. 17. For each band, the measured and simulated correlation coefficients show a good agreement with each other.

## V. CONCLUSIONS

In this paper, we have conducted massive MIMO channel measurements at 11, 16, 28, and 38 GHz frequency bands in an indoor office environment. The measurement data have been processed with the SAGE algorithm and important channel statistical properties like APDP, PAP, PEP, RMS DS, AAS, EAS, and their CDFs and correlation properties have been obtained and compared for the four bands. The new propagation characteristics caused by large antenna array have been validated for 10–40 GHz mmWave bands. Especially, the spherical wavefront property, cluster birth-death property, and the non-stationarity over the array have been verified by investigating the temporal-spatial MPC parameter variations over the array, including the PDP, PAP, and PEP. The variations of statistical properties such as DS, AAS, and EAS have also been characterized. The channel capacities of different bands have been obtained. The measurements have been validated by the PG model and GBSM. These mmWave massive MIMO channel measurements and analysis have indicated that massive MIMO propagation characteristics should be considered for mmWave channel modeling under large antenna array systems.

## REFERENCES

[1] T. S. Rappaport *et al.*, "Millimeter wave mobile communications for 5G cellular: It will work!" *IEEE Access*, vol. 1, pp. 335–349, May 2013.
[2] C.-X. Wang *et al.*, "Cellular architecture and key technologies for 5G wireless communication networks," *IEEE Commun. Mag.*, vol. 52, no. 2, pp. 122–130, Feb. 2014.
[3] *METIS Website*, accessed on Oct. 23, 2016. [Online]. Available: https://www.metis2020.com/
[4] *MIWEBA Website*, accessed on Oct. 23, 2016. [Online]. Available: http://www.miweba.eu/#Start
[5] *mmMAGIC Website*, accessed on Oct. 23, 2016. [Online]. Available: https://5g-mmmagic.eu/
[6] *5GCM Website*, accessed on Oct. 23, 2016. [Online]. Available: http://www.5gworkshops.com/5GCM.html
[7] *3GPP Website*, accessed on Oct. 23, 2016. [Online]. Available: http://www.3gpp.org/DynaReport/38900.htm
[8] *NG60 Website*, accessed on Oct. 23, 2016. [Online]. Available: http://www.ieee802.org/11/Reports/ng60_update.htm
[9] *NYU Wireless Website*, accessed on Oct. 23, 2016. [Online]. Available: http://wireless.engineering.nyu.edu/nyusim/
[10] M. Kim, J.-I. Takada, Y. Chang, J. Shen, and Y. Oda, "Large scale characteristics of urban cellular wideband channels at 11 GHz," in *Proc. EuCAP*, Lisbon, Portugal, Apr. 2015, pp. 1–4.
[11] X. Zhou *et al.*, "Experimental characterization and correlation analysis of indoor channels at 15 GHz," *Int. J. Antennas Propag.*, vol. 2015, May 2015, Art. no. 601835.
[12] M. Lei, J. Zhang, T. Lei, and D. Du, "28-GHz indoor channel measurements and analysis of propagation characteristics," in *Proc. PIMRC*, Washington, DC, USA, Sep. 2014, pp. 208–212.
[13] X. Yin, C. Ling, and M.-D. Kim, "Experimental multipath-cluster characteristics of 28-GHz propagation channel," *IEEE Access*, vol. 3, no. 1, pp. 3138-–3150, Jan. 2016.
[14] S. Hur *et al.*, "Wideband spatial channel model in an urban cellular environments at 28 GHz," in *Proc. EuCAP*, Lisbon, Portugal, Apr. 2015, pp. 1–5.
[15] I. Rodriguez *et al.*, "Analysis of 38 GHz mmWave propagation characteristics of urban scenarios," in *Proc. Eur. Wireless*, Budapest, Hungary, May 2015, pp. 1–8.

[16] J. Zhu, H. Wang, and W. Hong, “Large-scale fading characteristics of indoor channel at 45-GHz band,” *IEEE Antennas Wireless Propag. Lett.*, vol. 14, pp. 735–738, Dec. 2014.

[17] S. Wyne, K. Haneda, S. Ranvier, F. Tufvesson, and A. F. Molisch, “Beamforming effects on measured mm-wave channel characteristics,” *IEEE Trans. Wireless Commun.*, vol. 10, no. 11, pp. 3553–3559, Nov. 2011.

[18] K. Haneda, J. Järveläinen, A. Karttunen, M. Kyrö, and J. Putkonen, “A statistical spatio-temporal radio channel model for large indoor environments at 60 and 70 GHz,” *IEEE Trans. Antennas Propag.*, vol. 63, no. 6, pp. 2694–2704, Jun. 2015.

[19] T. S. Rappaport, E. Ben-Dor, J. N. Murdock, and Y. Qiao, “38 GHz and 60 GHz angle-dependent propagation for cellular & peer-to-peer wireless communications,” in *Proc. IEEE ICC*, Ottawa, Canada, Jun. 2012, pp. 4568–4573.

[20] Y. Azar *et al.*, “28 GHz propagation measurements for outdoor cellular communications using steerable beam antennas in New York city,” in *Proc. IEEE ICC*, Budapest, Hungary, Jun. 2013, pp. 5143–5147.

[21] G. R. MacCartney and T. S. Rappaport, “73 GHz millimeter wave propagation measurements for outdoor urban mobile and backhaul communications in New York city,” in *Proc. IEEE ICC*, Sydney, NSW, Australia, Jun. 2014, pp. 4862–4867.

[22] L. Lu, G. Y. Li, A. L. Swindlehurst, A. Ashikhmin, and R. Zhang, “An overview of massive MIMO: Benefits and challenges,” *IEEE J. Sel. Topics Signal Process.*, vol. 8, no. 5, pp. 742–758, Oct. 2014.

[23] H. Wei, D. Wang, J. Wang, and X. You, “Impact of RF mismatches on the performance of massive MIMO systems with ZF precoding,” *Sci. China Inf. Sci.*, vol. 59, no. 2, pp. 26–39, Feb. 2016.

[24] X. Gao, O. Edfors, F. Rusek, and F. Tufvesson, “Massive MIMO performance evaluation based on measured propagation data,” *IEEE Trans. Wireless Commun.*, vol. 14, no. 7, pp. 3899–3911, Jul. 2015.

[25] C.-X. Wang, S. Wu, L. Bai, X. You, J. Wang, and C.-L. I, “Recent advances and future challenges for massive MIMO channel measurements and models,” *Sci. China Inf. Sci.*, vol. 59, no. 2, pp. 1–16, Feb. 2016.

[26] S. Payami and F. Tufvesson, “Channel measurements and analysis for very large array systems at 2.6 GHz,” in *Proc. EuCAP*, Prague, Czech Republic, Mar. 2012, pp. 433–437.

[27] X. Gao, F. Tufvesson, O. Edfors, and F. Rusek, “Measured propagation characteristics for very-large MIMO at 2.6 GHz,” in *Proc. ASILOMAR*, Pacific Grove, CA, USA, Nov. 2012, pp. 295–299.

[28] D. Fei, R. He, B. Ai, B. Zhang, K. Guan, and Z. Zhong, “Massive MIMO channel measurements and analysis at 3.33 GHz,” in *Proc. ChinaCom*, Shanghai, China, Aug. 2015, pp. 194–198.

[29] A. L. Swindlehurst, E. Ayanoglu, P. Heydari, and F. Capolino, “Millimeter-wave massive MIMO: The next wireless revolution?” *IEEE Commun. Mag.*, vol. 52, no. 9, pp. 56–62, Sep. 2014.

[30] S. Sur, V. Venkateswaran, X. Zhang, and P. Ramanathan, “60 GHz indoor networking through flexible beams: A link-level profiling,” in *Proc. ACM SIGMETRICS*, Portland, OR, USA, Jun. 2015, pp. 71–84.

[31] X. Wang, S. Mao, and M. X. Gong, “A survey of LTE Wi-Fi coexistence in unlicensed bands,” *Mobile Comput. Commun.*, vol. 20, no. 3, pp. 17–23, Jul. 2016.

[32] F. Boccardi, R. W. Heath, A. Lozano, T. L. Marzetta, and P. Popovski, “Five disruptive technology directions for 5G,” *IEEE Commun. Mag.*, vol. 52, no. 2, pp. 74–80, Feb. 2014.

[33] B. Ai *et al.*, “Challenges toward wireless communications for high-speed railway,” *IEEE Trans. Intell. Transp. Syst.*, vol. 15, no. 5, pp. 2143–2158, Oct. 2014.

[34] B. Ai *et al.*, “Future railway services-oriented mobile communications network,” *IEEE Commun. Mag.*, vol. 53, no. 10, pp. 78–85, Oct. 2015.

[35] A. Taira *et al.*, “Performance evaluation of 44 GHz band massive MIMO based on channel measurement,” in *Proc. Globecom*, San Diego, CA, USA, Dec. 2015, pp. 1–6.

[36] J. Chen, X. Yin, and S. Wang, “Measurement-based massive MIMO channel modeling in 13–17 GHz for indoor hall scenarios,” in *Proc. IEEE ICC*, Kuala Lumpur, Malaysia, May 2016, pp. 1–5.

[37] X. Wu *et al.*, “60-GHz millimeter-wave channel measurements and modeling for indoor office environments,” *IEEE Trans. Antennas Propag.*, vol. 65, no. 4, pp. 1912–1924, Apr. 2017.

[38] B. H. Fleury, M. Tschudin, R. Heddergott, D. Dahlhaus, and K. Ingeman Pedersen, “Channel parameter estimation in mobile radio environments using the SAGE algorithm,” *IEEE J. Sel. Areas Commun.*, vol. 17, no. 3, pp. 434–450, Mar. 1999.

[39] B. H. Fleury, P. Jourdan, and A. Stucki, “High-resolution channel parameter estimation for MIMO applications using the SAGE algorithm,” in *Proc. IZSBC*, Zürich, Switzerland, Feb. 2002, pp. 301–309.

[40] B. Nkakanou, G. Y. Delisle, and N. Hakem, “Experimental characterization of ultra-wideband channel parameter measurements in an underground mine,” *J. Comput. Netw. Commun.*, Art. 157596, 2011.

[41] M. K. Samimi and T. S. Rappaport, “3-D millimeter-wave statistical channel model for 5G wireless system design,” *IEEE Trans. Microw. Theory Techn.*, vol. 64, no. 7, pp. 2207–2225, Jul. 2016.

[42] L. Liu, D. W. Matolak, C. Tao, Y. Li, B. AI, and H. Chen, “Channel capacity investigation of a linear massive MIMO system using spherical wave model in LOS scenarios,” *Sci. China Inf. Sci.*, vol. 59, no. 2, pp. 40–54, Feb. 2016.

[43] S. Wu, C.-X. Wang, M. Aggoune, M. M. Alwakeel, and Y. He, “A non-stationary 3-D wideband twin-cluster model for 5G massive MIMO channels,” *IEEE J. Sel. Areas Commun.*, vol. 32, no. 6, pp. 1207–1218, Jun. 2014.

[44] T. Pedersen, G. Steinböck, and B. H. Fleury, “Modeling of reverberant radio channels using propagation graphs,” *IEEE Trans. Antennas Propag.*, vol. 60, no. 12, pp. 5978–5988, Dec. 2012.

[45] T. Pedersen and B. H. Fleury, “A realistic radio channel model based on stochastic propagation graphs,” in *Proc. 5th MATHMOD Vienna*, Vienna, Austria, Feb. 2006, pp. 324–331.

[46] S. Wu, C. X. Wang, H. Haas, E. H. M. Aggoune, M. M. Alwakeel, and B. Ai, “A non-stationary wideband channel model for massive MIMO communication systems,” *IEEE Trans. Wireless Commun.*, vol. 14, no. 3, pp. 1434–1446, Mar. 2015.

**Jie Huang** received the B.Sc. degree in information engineering from Xidian University, China, in 2013. He is currently pursuing the Ph.D. degree in communication and information systems with Shandong University, China. His current research interests include millimeter wave and massive MIMO channel measurements, parameter estimation, and channel modeling, and 5G wireless communications.

**Cheng-Xiang Wang** (S’01–M’05–SM’08–F’17) received the B.Sc. and M.Eng. degrees in communication and information systems from Shandong University, China, in 1997 and 2000, respectively, and the Ph.D. degree in wireless communications from Aalborg University, Denmark, in 2004.

He was a Research Fellow with the University of Agder, Grimstad, Norway, from 2001 to 2005, a Visiting Researcher with Siemens AG Mobile Phones, Munich, Germany, in 2004, and a Research Assistant with the Hamburg University of Technology, Hamburg, Germany, from 2000 to 2001. He has been with Heriot-Watt University, Edinburgh, U.K., since 2005, where he was promoted to a Professor in 2011. He is also an Honorary Fellow of the University of Edinburgh, U.K., and a Chair/Guest Professor of Shandong University and Southeast University, China. He has authored one book, one book chapter, and over 270 papers in refereed journals and conference proceedings. His current research interests include wireless channel modeling and (B)5G wireless communication networks, including green communications, cognitive radio networks, high mobility communication networks, massive MIMO, millimeter wave communications, and visible light communications.

Dr. Wang is a Fellow of the IET and HEA, and a member of the EPSRC Peer Review College. He served or is currently serving as an Editor for nine international journals, including the IEEE TRANSACTIONS ON VEHICULAR TECHNOLOGY since 2011, the IEEE TRANSACTIONS ON COMMUNICATIONS since 2015, and the IEEE TRANSACTIONS ON WIRELESS COMMUNICATIONS from 2007 to 2009. He was the leading Guest Editor of the IEEE JOURNAL ON SELECTED AREAS IN COMMUNICATIONS, Special Issue on Vehicular Communications and Networks. He is also a Guest Editor of the IEEE JOURNAL ON SELECTED AREAS IN COMMUNICATIONS, Special Issue on Spectrum and Energy Efficient Design of Wireless Communication Networks, and the IEEE TRANSACTIONS ON BIG DATA, Special Issue on Wireless Big Data. He served or is serving as a TPC Member, TPC Chair, and General Chair of over 80 international conferences. He received nine Best Paper Awards from the IEEE Globecom 2010, the IEEE ICCT 2011, ITST 2012, the IEEE VTC 2013, IWCMC 2015, IWCMC 2016, the IEEE/CIC ICCC 2016, and the WPMC 2016.

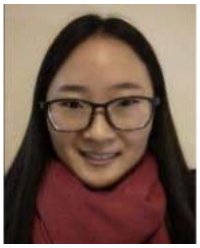

**Rui Feng** received the B.Sc. degree in communication engineering and the M.Eng. degree in signal and information processing from Yantai University, China, in 2011 and 2014, respectively. She is currently pursuing the Ph.D. degree with the School of Information Science and Engineering, Shandong University, China. Her research interests include channel parameter estimation, millimeter wave, and massive MIMO channel measurements and modeling.

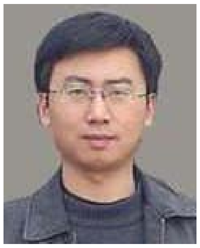

**Jian Sun** (M'08) received the Ph.D. degree from Zhejiang University, Hangzhou, China, in 2005. Since 2005, he has been a Lecturer with the School of Information Science and Engineering, Shandong University, China. In 2011, he was a Visiting Scholar with Heriot-Watt University, U.K., supported by the U.K.–China Science Bridges: Research and Development on (B)4G Wireless Mobile Communications (UC4G) Project. His research interests are in the areas of signal processing for wireless communications, channel sounding and modeling, propagation measurement and parameter extraction, MIMO, and multicarrier transmission systems design and implementation.

**Wensheng Zhang** (S'08–M'11) received the M.Eng. degree in electrical engineering from Shandong University, China, in 2005, and the Ph.D. degree in electrical engineering from Keio University, Japan, in 2011. In 2011, he joined the School of Information Science and Engineering, Shandong University, where he is currently an Associate Professor. His research interests lie in cognitive radio networks, random matrix theory, and visible light communications.

**Yang Yang** (S'99–M'02–SM'10) received the B.Eng. and M.Eng. degrees in radio engineering from Southeast University, Nanjing, China, in 1996 and 1999, respectively, and the Ph.D. degree in information engineering from The Chinese University of Hong Kong in 2002.

He has held faculty positions with the University College London, Brunel University, and The Chinese University of Hong Kong. He is currently a Professor with the Shanghai Institute of Microsystem and Information Technology, Chinese Academy of Sciences, where he is currently serving as the Director of CAS Key Laboratory of Wireless Sensor Network and Communication, and the Director of Shanghai Research Center for Wireless Communications. He is also a Distinguished Adjunct Professor with the School of Information Science and Technology, ShanghaiTech University. He has authored over 150 papers and filed over 80 technical patents in wireless communications. His current research interests include wireless sensor networks, Internet of Things, fog computing, open 5G, and advanced wireless testbeds.

Dr. Yang is a member of the Chief Technical Committee of the National Science and Technology Major Project New Generation Mobile Wireless Broadband Communication Networks (2008–2020), which is funded by the Ministry of Industry and Information Technology, China. He is also on the Chief Technical Committee of the National 863 Hi-Tech Research and Development Program 5G System Research and Development Major Projects, which is funded by the Ministry of Science and Technology, China. Since 2017, he has been serving the OpenFog Consortium as the Director of the Greater China Region.